On-orbit direction-finding of lightning

radio-frequency emissions recorded by

the FORTE satellite

Abram R. Jacobson (corresponding author)
&
Xuan-Min Shao

Space and Atmospheric Sciences Group
Mail Stop D466
Los Alamos National Laboratory
Los Alamos, New Mexico 87545   USA
(505)667-9656
ajacobson@lanl.gov

Abstract

The recording of radiofrequency signals from space potentially provides a means for global, near-real-time remote sensing of vigorous convective storms and a possible early-warning system for convection-associated severe weather. In general, radiofrequency signals arriving at a satellite with modest antenna gain do not directly reveal the ground location of those signals' source. We develop here a means of inferring the source location using repeated signal recordings from the same source storm, with the successive recordings taken along a significant segment of the satellite pass in view of the storm. The method is based on the ratio of received power on each of a pair of crossed dipole antennas. This method has a positional accuracy of 100-500 km. Moreover, the method has an intrinsic right-left (with respect to the subsatellite track) location ambiguity. A promising use of this technique in future applications will be as an aid in assigning lightning RF-emission sources to meteorological features from other global remote-sensing products, for example satellite infrared imagery of clouds.

Background

Space-based monitoring of lightning emissions is gaining importance as an efficient means of tracking convective storms globally. Satellite-borne optical imagers [*Boccippio et al.*, 2001; *Boccippio et al.*, 2000; *Boccippio et al.*, 1999; *Christian et al.*, 1999; *Suszcynsky et al.*, 2000] provide straightforward geolocation of lightning regions via image registration onto the ground. Their pixel resolution, on the order of 10 km, allows identification of convective cells.

By contrast, lightning radio-frequency (RF) signals observed in space are not able, by themselves, to reveal on a single-shot basis the location of a lightning storm to better than an uncertainty of thousands of km. This is because a typical lightning frequency, say 30MHz, has a wavelength (10 m) larger than the antenna aperture, precluding significant antenna angular directivity.

Recording of lightning RF emissions from a convective storm would be most useful if the storm's location, meteorological setting and basic parameters were known. For example, the vertical "depth" of the convective storm can be monitored via the retrieved height of the RF emission; this height is retrievable from RF data only if the storm's geographic location is somehow known by other means, and is retrieved via the time delay of ground-reflected RF pulses [*Jacobson et al.*, 1999]. In the case that a storm's location is known and that the storm causes lightning emissions received in space, the RF data then becomes a useful monitor of the depth of convection (reaching, in the extreme, cloud and mixed-phase electrification extending to near the tropopause, and sometimes overshooting into the stratosphere). Deep convection is usually a prerequisite for the

occurence of severe weather phenomena such as large hail, tornadoes, and intense microburst winds [*Williams et al.*, 1989].

Space-based recording of radio-frequency signals from lightning has been performed by two research satellites. The first satellite, Alexis, carried the Blackbeard radio-receiver payload developed by W. T. Armstrong [*Holden et al.*, 1995]. Blackbeard had one receiving channel and recorded the signal from a single antenna during any given recording. The recording limit was typically one, or at most two, RF lightning events per storm. The FORTE satellite [*Jacobson et al.*, 1999] is able to record hundreds of RF lightning signals from the same storm, during the entire duration of FORTE visibility from the storm. This has allowed the storm's geolocation to be inferred cumulatively (from all those events) using the time-dependence of the ionospheric slant-path total electron content (TEC) derived from the signal dispersion [*Jacobson et al.*, 1999; *Tierney et al.*, 2001]. This method assumes horizontally homogeneous ionospheric condtions. Location accuracies on the order of 100-500 km can be obtained by that technique *when the ionosphere is indeed uniform horizontally.* However, horizontal gradients in the ionospheric conditions (height, density, thickness) can seriously confuse this approach and can lead to faulty inferred storm geolocations.

More recently, methods exploiting the geomagnetic RF birefringence of the ionosphere have been developed for inferring source location. These methods exploit the birefringent mode splitting that is visible on sufficiently narrow RF pulses (width < 3 μs or so). The simpler approach requires that the satellite record three or more recurrent emissions from

the same storm, and then uses a geomagnetic model to infer the storm location from the birefringent mode splitting in the recorded signals [*Jacobson and Shao*, 2001b] with 100-500 km accuracy. A more elegant approach uses FORTE's coherent recording of two signals simultaneously, one from each of two crossed dipole antennas [*Shao and Jacobson*, 2001]. This approach is capable of approximately geolocating a storm from a single-event RF signal coherently recorded on both antennas, although the statistical strength of that geolocation is further improved by averaging over multiple, time-separated events. However, either of the geomagnetic-birefringence approaches have particular difficulty geolocating storms near the equator where the satellite is approximately overhead relative to the source, because the geomagnetic field is nearly normal to the satellite/source line-of-sight, and the mode-splitting therefore becomes impractically small [*Jacobson and Shao*, 2001b; *Shao and Jacobson*, 2001]. This is especially unfortunate for locating lightning, because the tropics provide most of the lightning detectable from space.

The remainder of this article will deal with data from the FORTE satellite, whose operations and RF-data capability and characteristics have been described in detail elsewhere [*Jacobson et al.*, 2000; *Jacobson et al.*, 1999; *Jacobson and Shao*, 2001a; *Jacobson and Shao*, 2001b; *Light et al.*, 2001; *Massey et al.*, 1998b; *Shao and Jacobson*, 2001; *Tierney et al.*, 2001].

The concept for direction-finding from space using a finite orbital segment

In order to provide a more robust technique for crossed-antenna satellite geolocation of storms, we now borrow from synthetic-aperture radar (SAR) the principle that although the satellite antenna is small, the satellite orbital arc (over which recurrent emissions are recorded from the same storm) may be very large. This allows the storm to be observed in a variety of vector angles in the two antennas' respective beamlobes. The *ratio of the two antennas' signals* can then be tracked in time (as the satellite travels along its orbit), and the time history of the ratio can be used to infer the storm location on Earth. (We do not mean to imply that the present technique relies on phase-coherence over the synthetic arc; we do not require coherent behavior of either the source, or the radio receiver, between repeated event recordings.) Since a lightning storm tends to produce detectable RF signals over most if not all of the duration of satellite visibility (from the storm) [*Jacobson et al.*, 2000; *Jacobson et al.*, 1999; *Tierney et al.*, 2001], the requirement for recurrent emissions is not at all limiting, as long as the goal is to locate lightning storms (as opposed to non-recurrent phenomena).

Figure 1 shows the scheme. The view is downward onto the satellite. The large circle is the Earth's limb as seen from the satellite. One dipole antenna (#2) is aligned toward the ram direction, tangent to the orbit. The other dipole antenna (#1) is at right angles to both the ram and nadir (earthward) directions. This is basically the arrangement of the primary antennas on FORTE [*Jacobson et al.*, 1999; *Jacobson and Shao*, 2001b]; the use of a broadband log-periodic antenna in place of each dipole does not essentially change this method at all. The coordinates in Figure 1 are nadir angle ϕ (reckoned from the

downward, or "nadir" direction) and azimuth θ (reckoned clockwise from the ram

direction.) FORTE is at slightly higher than 800 km altitude, so the Earth's limb is at

about 63 deg nadir angle. During much of its mission, FORTE operated with syncronous,

simultaneous recording of the RF signals on the two antennas, in an effective passband

26-48 MHz.

Figure 1: Satellite coordinate frame, looking downward onto the satellite. The large circle is the Earth's limb as seen from the satellite. One dipole antenna (#2) is aligned toward the ram direction, tangent to the orbit. The other dipole antenna (#1) is at right angles to both the ram and nadir (earthward) directions. The nadir direction is into the plane of the diagram. The coordinates in this satellite frame are nadir angle ϕ (reckoned nadir direction) and azimuth θ (reckoned clockwise from the ram direction.)
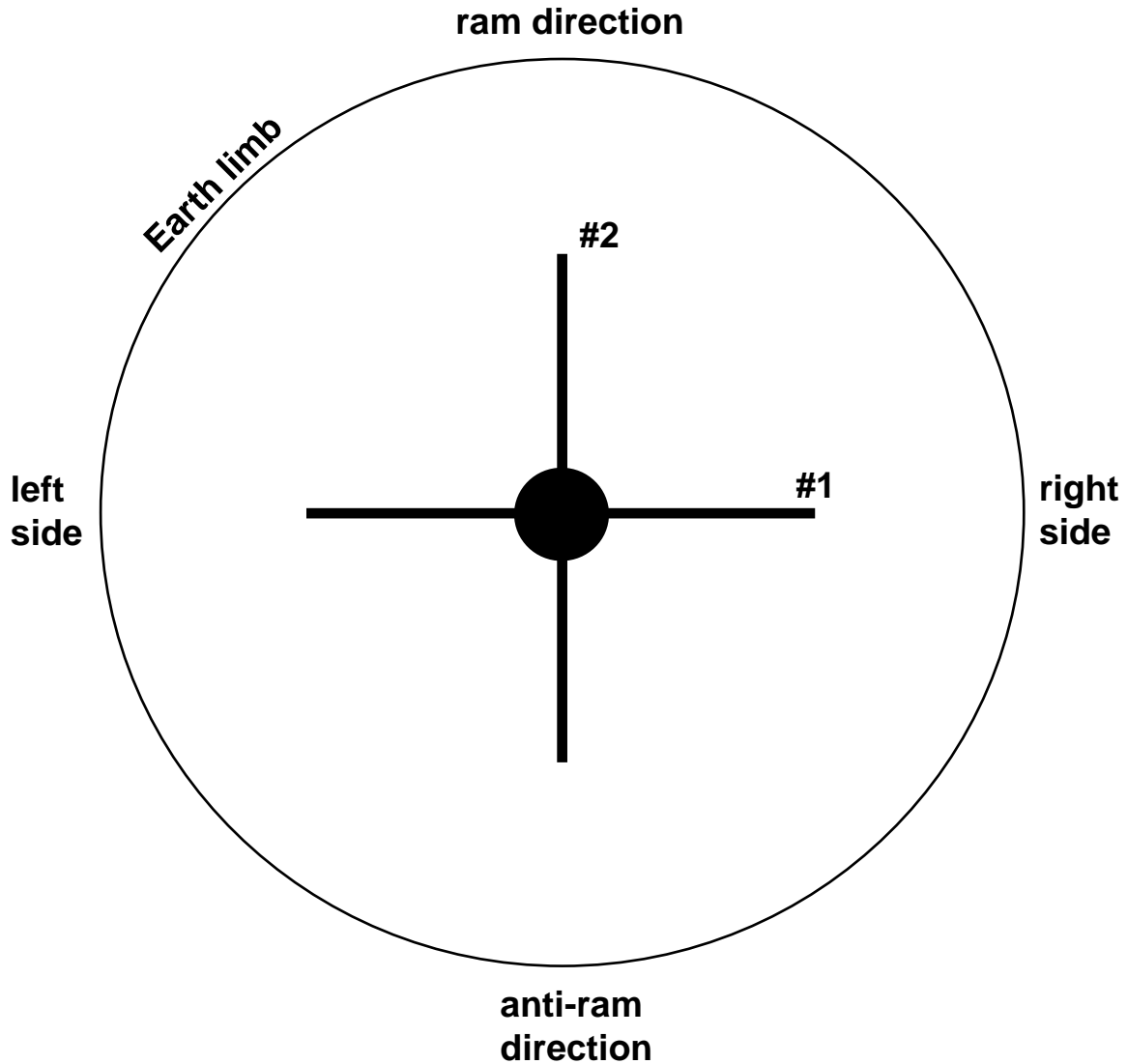
As FORTE passes a storm, the storm's satellite-frame angular position in Figure 1 migrates from the top of the figure toward the bottom. If we ignore Earth spin, then the

storm's trajectory in the satellite angular frame is exactly a straight line parallel to antenna #2. It is a serviceable approximation to ignore Earth spin in this case: FORTE's orbital inclination is 70 deg, so that the subsatellite track crosses the Earth's equator at a 70-deg angle. The Earth causes a storm at the equator to slip westward at ~470 m/s under the orbital plane. The component of this slip normal to the subsatellite track is ~440 m/s. Thus if a storm is observed for 5 minutes (300 s) during a FORTE pass, the storm drifts ~ 130 km normal to the orbit during the observation. We will return to that detail later. However, for the time being we point out that the curved diameter of the FORTE-viewed limb is >5000 km, so the blurring of the geolocation due to Earth spin is only ~3% of the potential ambiguity in position.

Let us define the "principal angles" of the dipole antennas #1 and #2 respectively:

$$
\begin{aligned}
\tan \alpha_1 &= |\sin \theta| \tan \phi \\
\tan \alpha_2 &= |\cos \theta| \tan \phi
\end{aligned}
\tag{1}
$$

where θ is the azimuth and ϕ is the nadir angle (in satellite coordinates). The meaning of principal angle is as follows: Define the antenna "E plane" as that plane containing both the nadir direction (vector from satellite to center of Earth) and the antenna element. Project an arbitrary three-dimensional line-of-sight (from the satellite to the RF emitter) into that plane. This we shall call the E-plane-projected line-of-sight. The angle between the E-plane-projected line-of-sight, and the nadir direction, is the principal angle. For a

dipole antenna in free space, the antenna lobe depends only on the principal angle, and the lobe is cylindrically symmetric around the antenna element (holding principal angle constant). The free-space dipole has a null at $\alpha = \pm 90$ deg. The FORTE LPA system [*Shao and Jacobson*, 2001] retains the dipole's property of having an approximate null near $\alpha = \pm 90$ deg, and while not perfectly cylindrically symmetric, the LPA lobe has very weak dependence on the rotation angle at least in the angular range (± 60 deg) subtended by the Earth.

Plate 1 shows the satellite-frame trajectory of a storm location on Earth in terms of the LPA power-response lobes (color-coded). We are assuming that the incoming electromagnetic radiation is randomly polarized, in which case the antenna response depends only on the line-of-sight direction [*Shao and Jacobson*, 2001]. In each panel (a, b, and c) the horizontal axis is α_1 and the vertical axis is α_2. Plate 1(a) shows the power response lobe for antenna #1, Plate 1(b) shows the power-response lobe for antenna #2, and Plate 1(c) shows the ratio of #1/#2. On each panel are superimposed as solid black lines the trajectory of a hypothetical storm (ignoring Earth spin). The dashed lines show the relatively small effect of Earth spin on this trajectory. The trajectory is shown as either right or left of the satellite track, as this makes no difference in the power response if we ignore Earth spin.

Plate 1: Antenna sensitivity (power-response lobes) in the plane containing the two dipoles. Horizontal axis is the cross-track principal angle, while vertical axis is the along-track principal angle. The ram direction is therefore upward in the page. Solid lines show right/left-symmetric tracks of a pair of points fixed on the ground. Dashed lines show the slightly asymmetric modification of these tracks due to Earth rotation. (a) Power-response lobe for antenna #1. (b) Power-response lobe for antenna #2. (c) Ratio of power-response lobes, #1/#2.
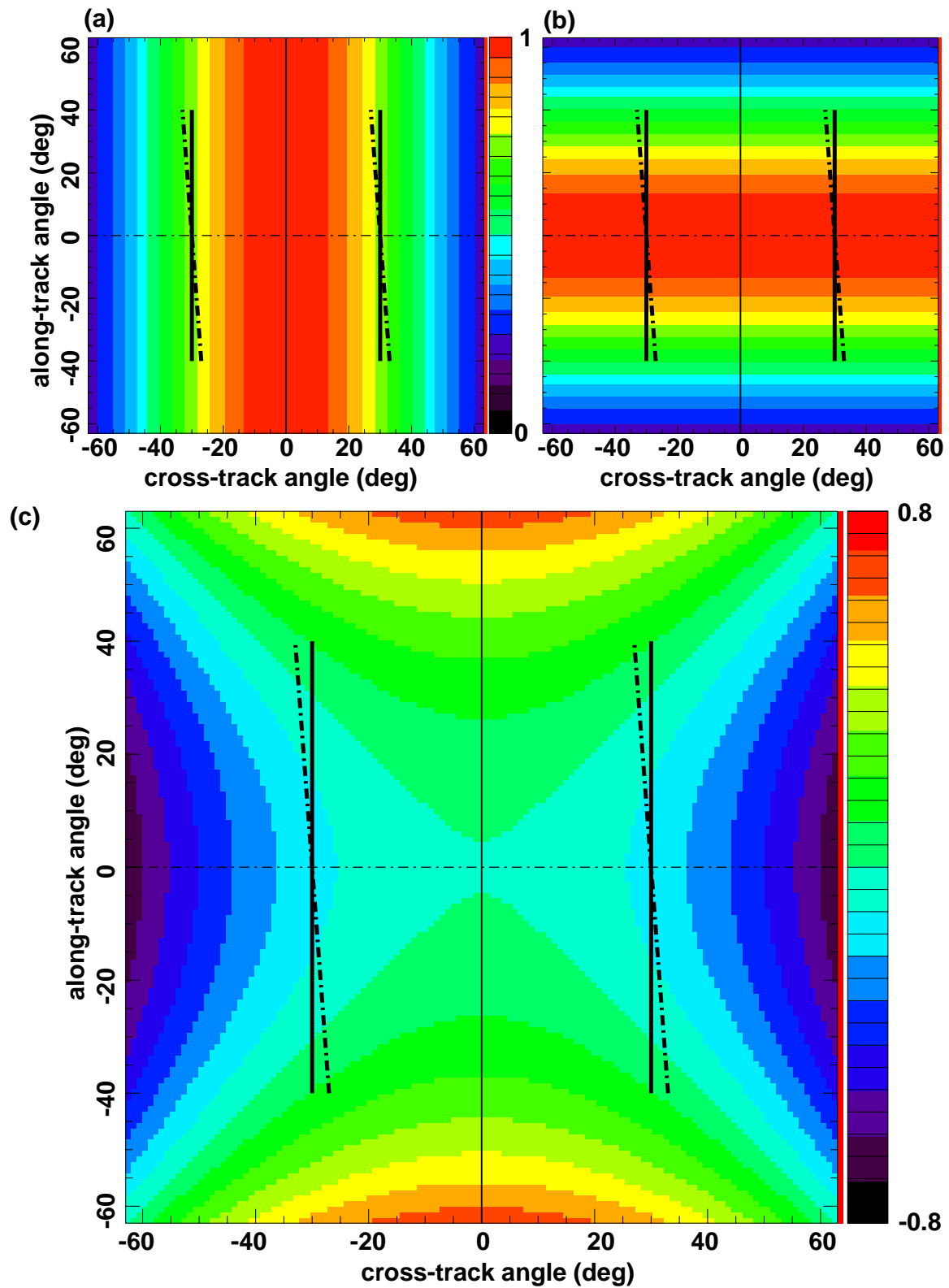
Plate 1(c) shows the predicted power *ratio*. This is the useful observable from our two-antenna recordings of randomly-polarized radiation from lightning. By taking the ratio, we can work with unpredictable, shot-to-shot varying lightning-emission powers and still infer the line-of-sight trajectory in the principal-angles plane over a sequence of emissions, at least to within a twofold (right/left) ambiguity. While a single received emission's #1/#2 power ratio does not provide sufficient information to locate the emission source, a series of emissions' power ratios (from the same source), distributed over enough range in time, does allow us to infer the location, albeit with right-left ambiguity.

The role of polarization

Our ability to geolocate lightning sources using this crossed-antenna power-ratio technique depends critically on the radiation's being randomly polarized. We will show that lightning RF emission pulses' degree of polarization can usually be inferred on the basis of an easily measured corrolary property. (In other cases the degree of polarization can be rigorously determined by a formal retrieval of the Stokes parameters [*Shao and Jacobson*, 2001].) First, though, we illustrate the importance of polarization in the interpretation of crossed-antenna data.

Figure 2 shows what we mean by linearly polarized versus randomly polarized. Figure 2(a) shows the radiation pattern (dashed lobe) of a single radiating dipole current element (heavy solid line). Figure 2(b) shows the situation with a "randomly polarized" emission source, consisting of an overlay of individual dipoles that are randomly oriented and randomly timed (with respect to each other). Although each elementary dipole emitter in the randomly-polarized case gives rise to polarized radiation considered individually, the radiation *from the ensemble of such emitters* is randomly polarized [*Born and Wolf*, 1975], i.e. as time progresses the polarization erratically jumps around in angle and approaches a mean of zero over a practical signal-averaging interval [*Shao and Jacobson*, 2001].

Figure 2: (a) The radiation pattern (dashed lobe) of a single radiating dipole current element (heavy solid line). (b) The situation with a "randomly polarized" emission source, consisting of an overlay of individual dipoles that are randomly oriented and randomly timed (with respect to each other). Although each elementary dipole emitter in the randomly-polarized case gives rise to polarized radiation considered individually, the radiation *from the ensemble of such emitters* **is randomly polarized.**

(a)

null

null

(b)
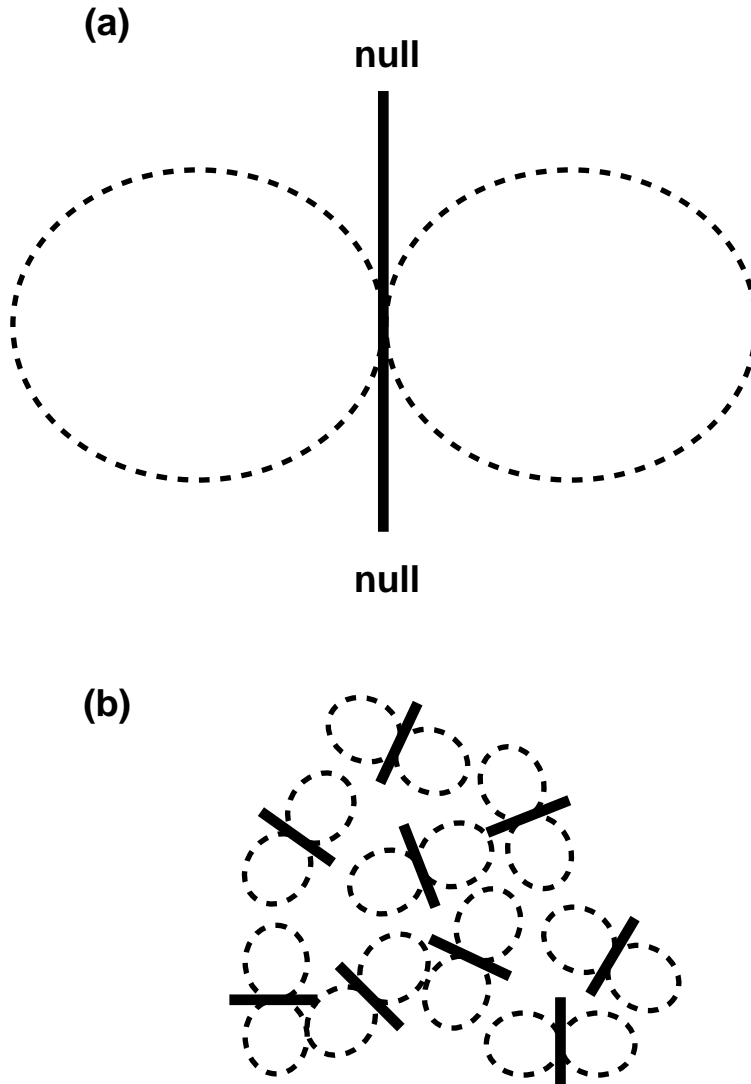
Typical lightning leader development displays a tortuous path [*Rhodes et al.*, 1994; *Shao and Krehbiel*, 1996; *Shao et al.*, 1995]. Moreover, we know from both theory [*Gallimberti*, 1979] and laboratory experiments on long-gap air discharges [*Group*, 1974] that each leader step's initiation is associated with multiple, angularly-diverse corona breakdowns starting from the leader tip. Owing to its ~1-10-nanosecond timescale, corona is a copious very-high-frequency (VHF; 30-300 MHz) emitter, and thus we expect much of the VHF emissions from lightning leader development to be randomly polarized, due to the appearance of mutiple corona events at largely random angles and at mutually-random timings. Thus, Figure 2(b) illustrates the type of emission we expect for corona accompanying most leader development. However, we add that not all lightning VHF emissions need be unpolarized [*Jacobson and Shao*, 2001a], and it will be necessary to apply the crossed-antenna direction-finding program selectively.

We now show in detail why polarized VHF should *not* be used as input data in crossed-antenna direction-finding. Figure 3 shows the "plane of incidence", containing the satellite, the nadir direction, and the lightning emitter. The emitter illuminates the satellite via a direct path, and also via a ground reflection [*Jacobson et al.*, 1999], which also lies within the plane of incidence. Considering this plane, the orientation of a single polarized emitter can be either "s" or "p" [*Born and Wolf*, 1975], meaning respectively either

normal to, or in, the plane of incidence. Figure 3 shows the case of "s" polarization, with

the emitting dipole pointed into the page, normal to the plane of incidence. The ground

reflection is equivalent to a virtual emitter under the Earth's surface; this virtual emitter is

also "s"-polarized. The satellite is in the cylindrically-symmetric maximum of both the

emitter's and the virtual emitter's lobes.

Figure 3: The "plane of incidence", containing the satellite, the nadir direction, and the lightning emitter, for an *s*-polarized emitter. The emitter illuminates the satellite via a direct path, and also via a ground reflection, which also lies within the plane of incidence.
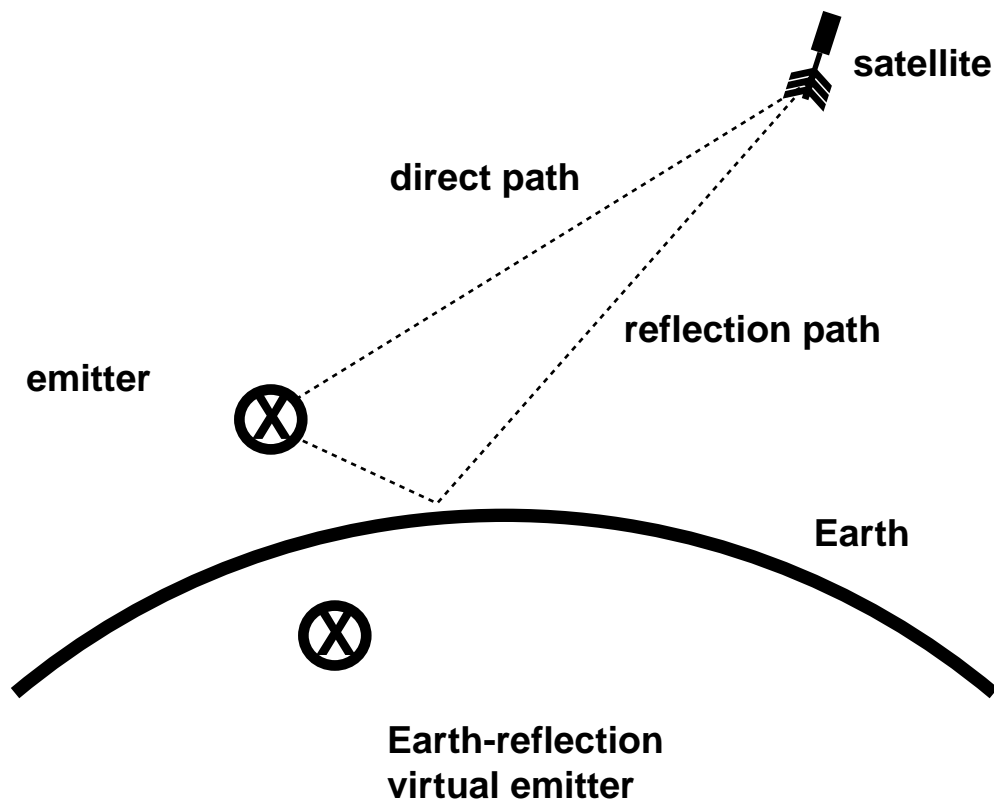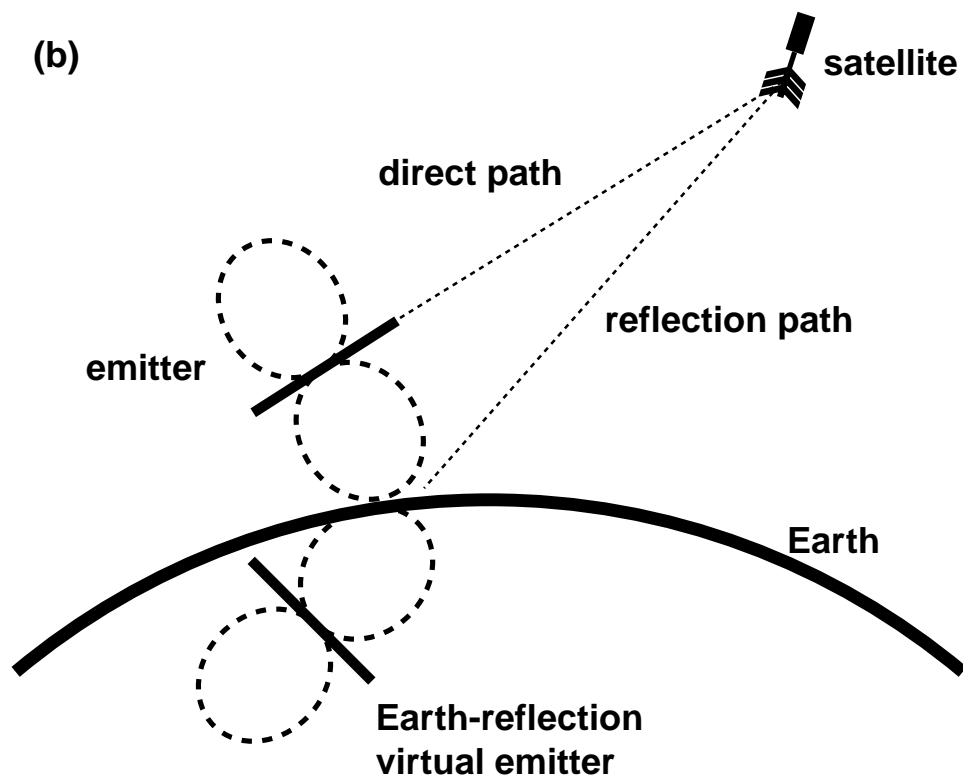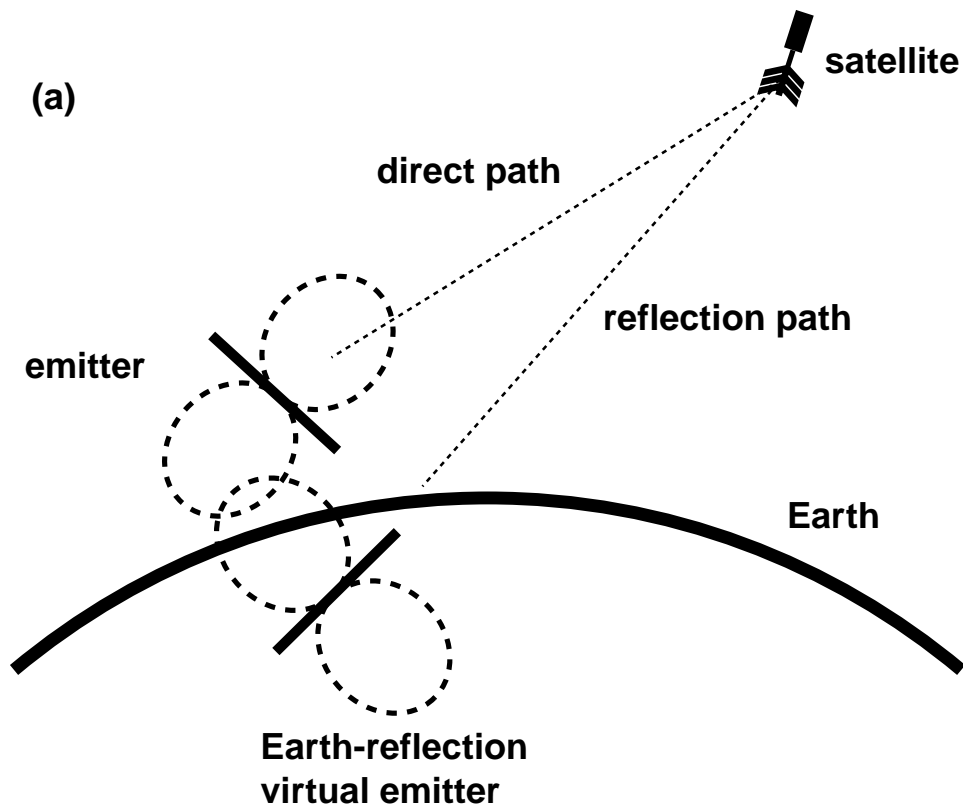

We will specialize to a particular case in order to make the argument as clear as possible,

but a similar argument can be made in more general conditions. Let the incidence plane

in Figure 3 also be normal to the satellite's ram direction. In other words, the plane

16

contains the satellite during the instant in its orbit of closest approach to the emitter. Thus, the emitter dipole in Figure 3 is parallel to antenna #2 and normal to antenna #1. This means that only antenna #2 will detect the signal. This would utterly defeat the antenna-lobe-ratio technique. The ratio of power on #1 to power on #2 would be identically zero, no matter what the offset of the emitter from the orbit, whenever the satellite is at closest approach to the emitter, given an s-polarized source dipole. This indicates one way in which the use of polarized emitters will tend to frustrate an interpretation of power-ratio information in terms simply of source location.

The ratio techniqe will also fail for a p-polarized dipole. Figure 4 shows two extreme cases of p-polarization: (a) satellite lies in maximum of direct emission lobe, and (b) satellite lies in null of direct emission lobe. In either case, only antenna #1 is sensible to the radiation, while antenna #2 is normal to the radiation and therefore detects no signal. Thus the ratio #1/#2 will be indeterminate (i.e., infinite) regardless of the satellite miss-distance at closest approach. Again, this will frustrate any attempt to infer the satellite miss-distance using an antenna-ratio technique.

Figure 4: For a *p*-polarized emitter, there are two extremes of orientation of the emitter. (a) Emitter radiation maximum directed toward satellite (and Earth-reflection virtual emitter's radiation null directed toward satellite). (b) Emitter radiation null directed toward satellite (and Earth-reflection virtual emitter's radiation maximum directed toward satellite).

(a)

satellite

direct path

reflection path

emitter

Earth

Earth-reflection
virtual emitter

(b)

satellite

direct path

reflection path

emitter

Earth

Earth-reflection
virtual emitter

Furthermore, a curious feature of p-polarized geometry is that the virtual emitter's

orientation is still p-polarized but is now shifted by 90 deg relative to the original emitter.

Thus, in Figure 4(a) the virtual emitter has a null toward the satellite, while in Figure 4(b)

the virtual emitter has a maximum toward the satellite. We believe this is the reason why

some "transionospheric pulse pairs", or TIPPs [*Holden et al.*, 1995; *Jacobson et al.*,

2000; *Jacobson et al.*, 1999; *Jacobson and Shao*, 2001a; *Massey and Holden*, 1995;

Massey et al., 1998a], have a second pulse stronger than the first pulse.

Having argued that polarized emissions can be expected *a priori* to frustrate the

attempted crossed-antenna power-ratio method, we now illustrate this point with case

examples of both polarized and unpolarized emissions. This illustration will also convey

the data-reduction method used in the power-ratio approach to geolocation of lightning

storms.

Plate 2 shows data from a series of narrow-pulse intracloud emissions. The top two

panels are spectrograms of relatively faint, narrow-pulse intracloud signals recorded from

orthogonal antennas (a) #2 and (b) #1. Some of the pulses are ground-reflections of other

pulses. The spectrograms show the spectral density of the received electric field,

displayed as the logarithm (base 10) of $(V/m)^2$ per MHz. These spectrograms indicate

ionospheric dispersion and the presence of quasi-continuous-wave carriers. The first

analysis step is to correct for the dispersion, and apply an identical carrier-suppression

filter, to each of the two spectrograms, then to sum up the E^2 over frequency and present

the result versus time [*Jacobson et al.*, 1999]. The latter is shown in Plate 2(c), in which

the colors are blue for antenna #1 and red for antenna #2. It is immediately obvious that

the ratio of the two powers does not remain even approximately constant during the

record.

Plate 2: Case study of relatively *polarized* RF signal from lightning. (a) Spectrogram of E^2 received on antenna #2 versus time (horizontal axis) and frequency (vertical axis). The color scale indicates the logarithm (base 10) of E^2 in units $(V/m)^2$ per MHz. (b) Same but for antenna #1. (c) E^2 versus time, after dechirping and carrier suppression, for antennas #1 (blue) and #2 (red). The shift leftward (relative to the spectrograms) is due to the dechirping.
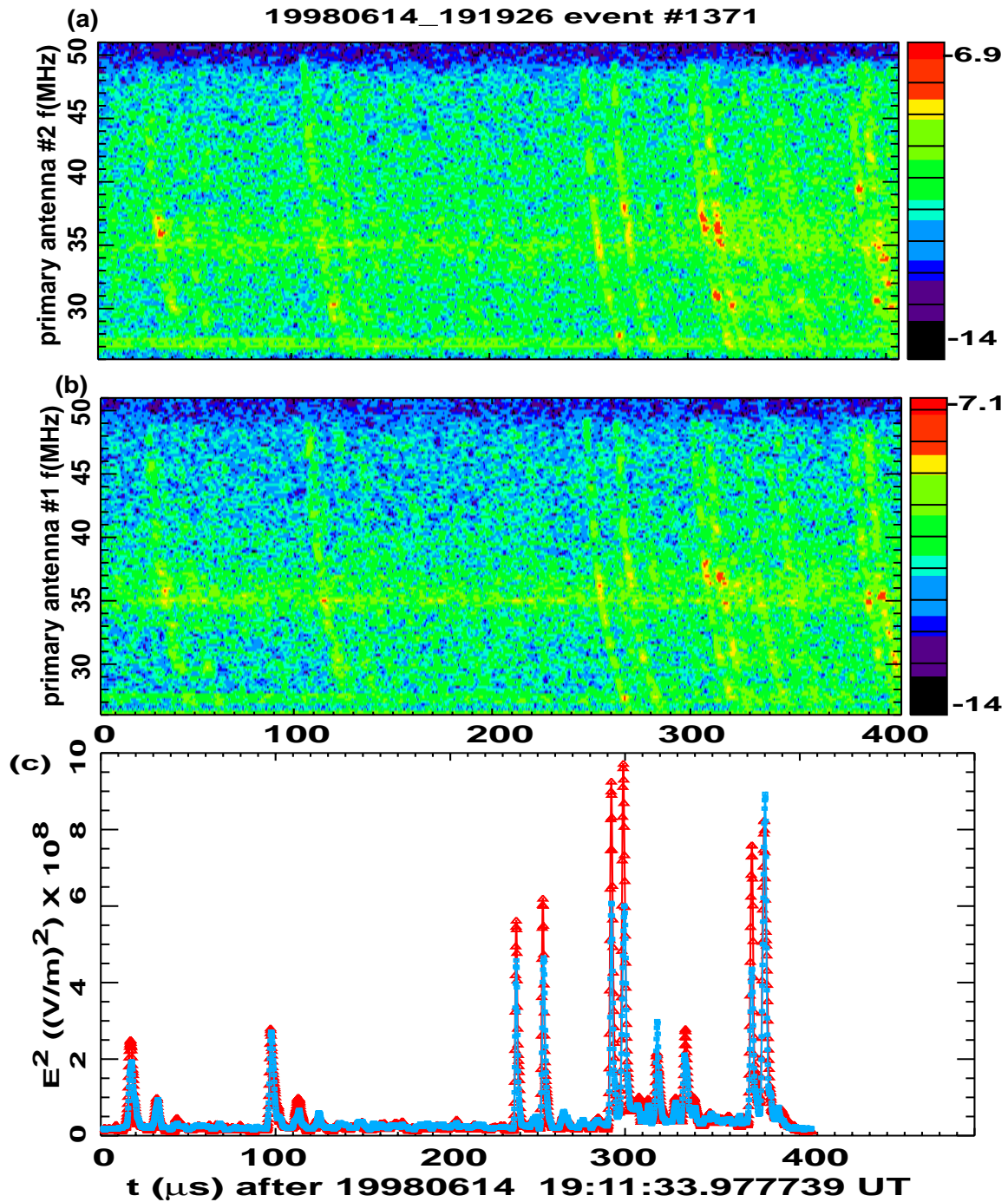
This is made clearer in Figure 5, which displays the 154 samples during which both antennas' signals exceed 20% of their respective maxima. (This selection compresses the data to include only the pulses, and to exclude the "dead time" between pulses.) Figure 5(a) shows the power for primary antenna #1 (squares) and antenna #2 (triangles). Figure 5(b) shows the ratio of #2 to #1. Evidently the power ratio is quite unstable during the succession of pulses in the record. Such data would not be suitable for use in power-ratio-based geolocation of storms. We point out that further analysis reveals that the intrinsic pulsewidths of the constituent pulses in this record are small, around 1 μs.

Figure 5: (a) E^2 versus sample-index number for antenna #2 (triangles) and antenna #1 (squares), for the 154 selected data points from Plate 2 (see text). (b) Corresponding ratio of #2/#1.
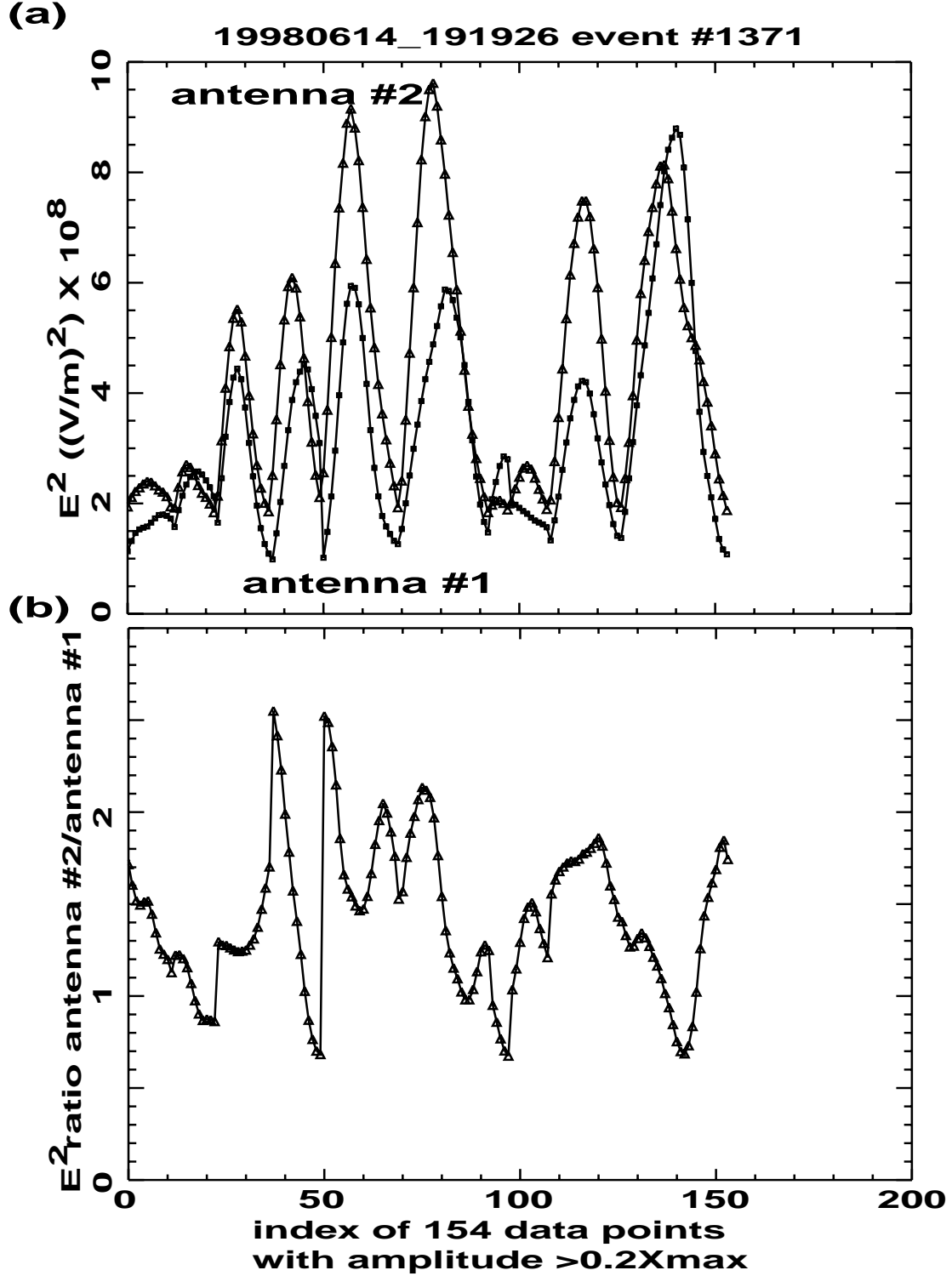

(a)

19980614_191926 event #1371

antenna #2

antenna #1

$E^2 ((V/m)^2) \times 10^8$

(b)

E^2ratio antenna #2/antenna #1

index of 154 data points
with amplitude >0.2Xmax

Plate 3 is analogous to Plate 2 and shows data for a pulse pair. The constituent pulses

have widths on the order of 5 μs, fivefold wider than in the previous example of Plate 2.

Figure 6 shows (a) E^2 versus time for both antennas, and (b) the #2/#1 power ratio versus

time, for the selected 96 samples in which both antennas' signals exceed 20% of their

respective maxima. Compared to the previous example, the power ratio is relatively

stable (though not perfectly constant) during the duration of the pulses. Evidently the case

of Plate 3 (and Figure 6) contains emissions that are more suitable for power-ratio

geolocation, relative to the previous case of Plate 2 (and Figure 5).

Plate 3: Case study of relatively *unpolarized* RF signal from lightning. (a) Spectrogram of E^2 received on antenna #2 versus time (horizontal axis) and frequency (vertical axis). The color scale indicates the logarithm (base 10) of E^2 in units $(V/m)^2$ per MHz. (b) Same but for antenna #1. (c) E^2 versus time, after dechirping and carrier suppression, for antennas #1 (blue) and #2 (red). The shift leftward (relative to the spectrograms) is due to the dechirping.
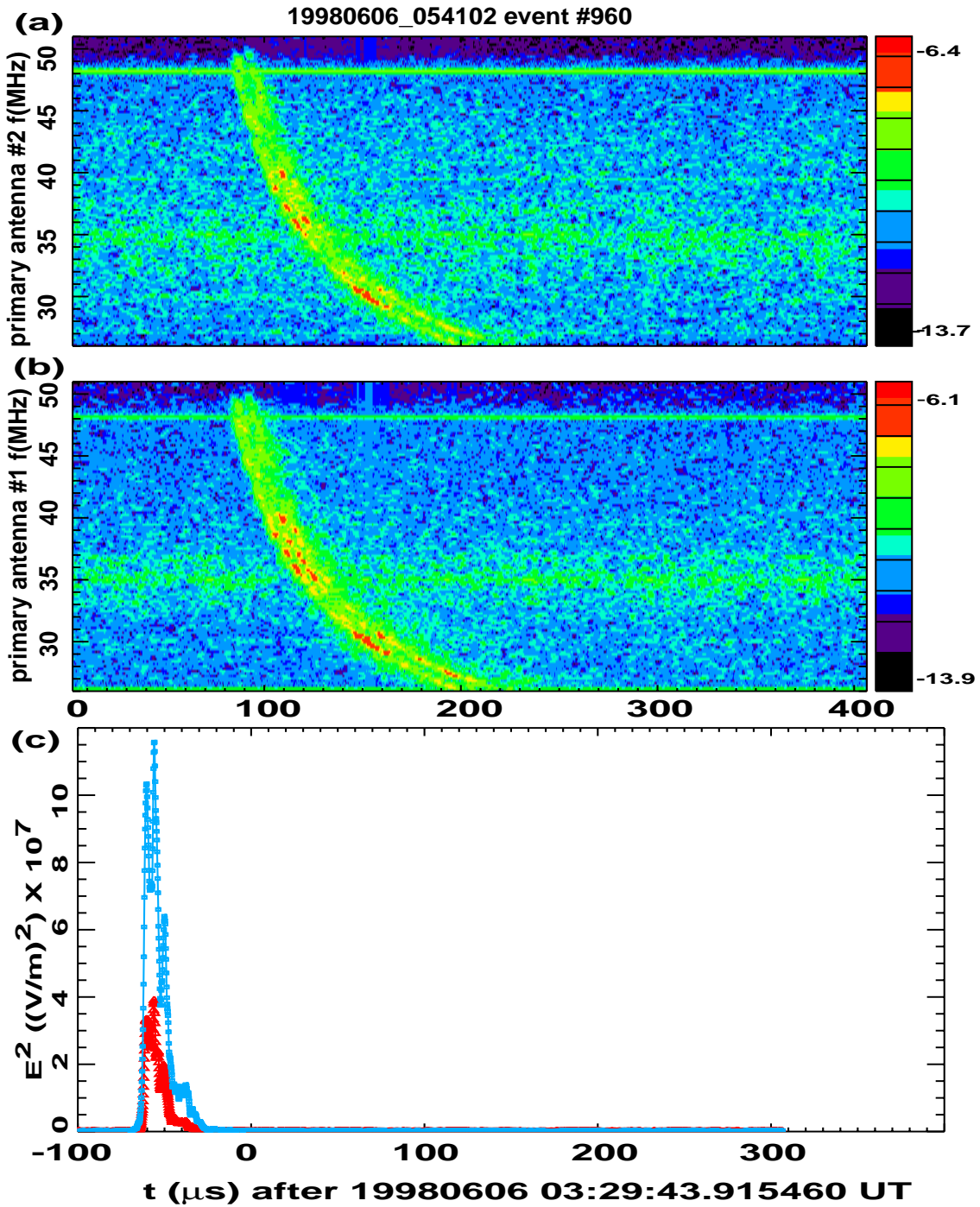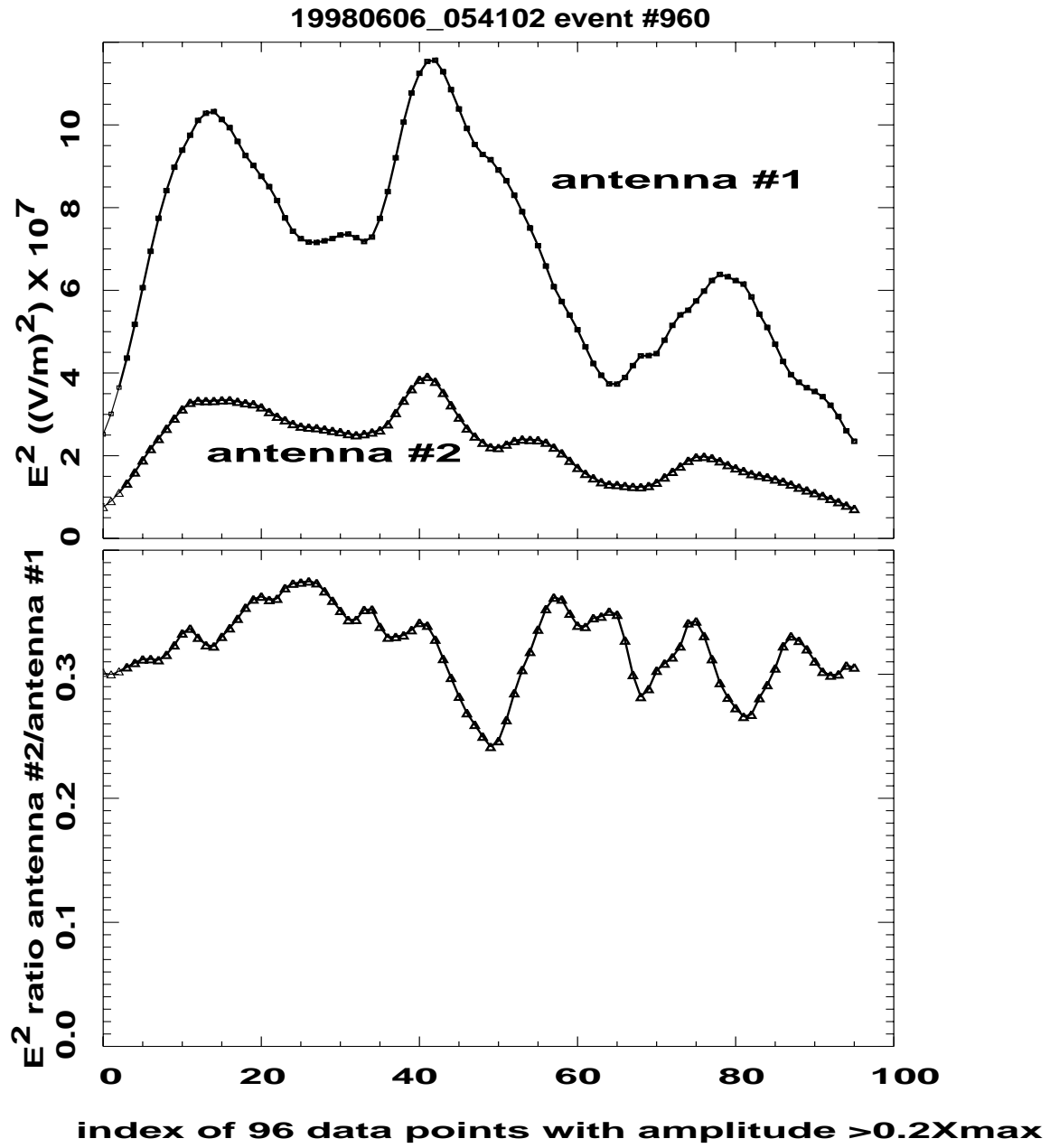
Figure 6: E^2 versus sample-index number for antenna #2 (triangles) and antenna #1 (squares), for the 96 selected data points from Plate 3 (see text). (b) Corresponding ratio of #2/#1.

19980606_054102 event #960

The pattern exhibited by these two case examples caused us to examine whether pulsewidth might serve as a usable proxy for degree of polarization. We have examined hundreds of other case examples, and have computed quantitative measures of polarization [*Jacobson and Shao*, 2001b; *Shao and Jacobson*, 2001] for those pulses. A general trend seems to characterize the FORTE VHF lightning data: *Emissions with characteristic pulsewidths on the order of 1 μs are often polarized, while emission with pulsewidths >3 μs are only rarely polarized.* Presumably the random polarization of the longer pulses is related either to a single radiating channel's tortuosity, or to the role of multiple, randomly-oriented emission dipoles (as in the case of corona in during air breakdown.) Therefore, in the work to follow, we pre-select data to include only those pulses having pulsewidths >3 μs. As a measure of pulsewidth, we use the power-autocorrelation-function 1/e width described elsewhere [*Jacobson et al.*, 1999]. While this selection criterion rejects some narrow-pulse (<3 μs) emissions that in fact are not polarized, we at least avoid too much contamination of the selected dataset by polarized emitters.

Empirical calibration of antenna-lobe ratio

During 1998 and 1999, FORTE undertook intensive collections of data over and near North America, in order to receive the benefit of ground-truthing by the National Lightning Detection Network [*Jacobson et al.*, 2000; *Jacobson and Shao*, 2001a]. Over the course of two summer-season campaigns, over 25-thousand FORTE VHF events

were identified as being associated with NLDN-located lightning strokes. Thus, these 25-thousand FORTE VHF events are associated with sources that are *a priori* geolocated, at least to within the ~97% certainty with which FORTE-NLDN correlations are valid [*Jacobson et al.*, 2000]. In addition to NLDN groundtruthing, coincident optical/VHF detections involving the optical imager aboard FORTE [*Light et al.*, 2001; *Suszcynsky et al.*, 2000] have provided another 10-thousand geolocations of FORTE VHF signal sources.

Together, these two sources of groundtruthing provide a candidate pool of 40-thousand FORTE VHF events for which we know reasonably well the signal's source location (latitude, longitude) on Earth, with something like 10-km resolution or better. Only about 15-thousand of these events had both antennas tuned to the same frequency, however; the rest had the two antennas tuned to different frequencies. We will consider only those 15-thousand events employing a single frequency, because the power-ratio method is possible only when both crossed antennas are looking at exactly the same frequency band. We next down-selected these events to arrive at those having both very strong signal-to-noise (peak power in pulse > 30X median power in record) and not too narrow autocorrelation width (1/e width > 3 μs), the latter in order to exclude polarized signals (see above). After imposing these two requirements, the pool of geolocated signals shrinks to 3,657 VHF events.

We now use those 3,657 selected events as a calibration set, in order to fit an empirical model of the antenna #1-to-antenna #2 power ratio. The data-reduction method that was

described earlier, in regard to Plates 2 and 3, is used for each of the 3,657 selected events.

Plate 4 shows the composite power-ratio results. Plate 4(a) graphs the power ratio

(vertical axis) as a function of line-of-sight azimuth in satellite coordinates (horizontal

axis; ram direction being azimuth=0). The color coding is for the line-of-sight nadir angle

in satellite coordinates, from blue at nadir directly underneath the satellite, to red at the

Earth's limb (63 deg). Plate 4(b) show the same data, this time color-coding the logarithm

(base 10) of the power ratio, in the range 0.1 (blue) to 4.0 (red), as a function of principal

angles α_1 and α_2 (see Eq. 1). Displayed in either way, there is an obvious trend for a

systematic azimuthal dependence of the power ratio, and this trend is accentuated by

increasing nadir angle. There are also a certain number of outliers in Plate 4. Their

number is within the expectation level (3%) of mistaken geolocations due to random

("false") NLDN/FORTE coincidences [*Jacobson et al.*, 2000].

Plate 4: Illustration of power-ratio results for 3,657 NLDN-geolocated RF emissions having pulsewidth > 3 μs and meeting other selection criteria (see text). (a) Power ratio (vertical axis) versus absolute value of satellite-frame azimuth (horizontal axis). The color scale indicates the satellite-frame nadir angle, from 0 deg (blue) to the Earth's limb at 63 deg (red). (b) Antenna #2 principal angle (vertical axis) versus antenna #1 principal angle (horizontal axis). The color scale marks the the logarithm (base 10) of the power ratio, in the range 0.1 (blue) to 4.0 (red).
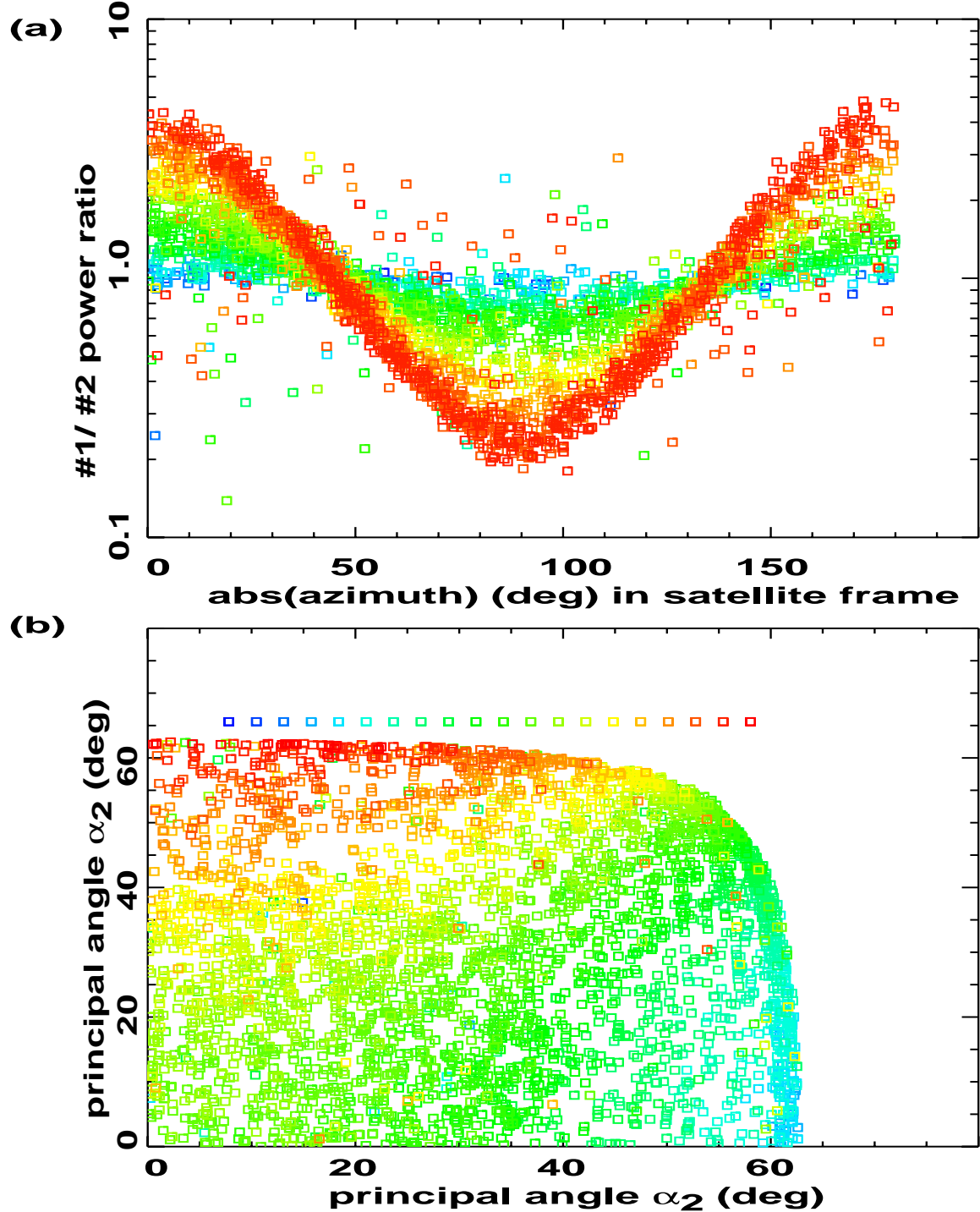
The 3,657 selected events' power ratios are next fitted to a separable function of the two principal angles, of the form [*Shao and Jacobson*, 2001]

$$ratio = \frac{\sin c^2(w\alpha_1)}{\sin c^2(w\alpha_2)} = \left(\frac{\sin(w\alpha_1)/(w\alpha_1)}{\sin(w\alpha_2)/(w\alpha_2)} \right)^2 \qquad (2)$$

where w is fitted. The best-fit value of w is 1.8, and the measured versus modeled power ratios are shown in Figure 7. The fit is good, to within a typical scatter of 0.03 in the logarithm (base 10) of the ratio. (Prior to the fit, a 10% power gain correction (of one antenna with respect to another) was applied to the data, as was indicated to be needed by the evidence of Plate 4.) As in Plate 4, the outliers are probably due to mistaken geolocations. In the work to follow, we will interpret power-ratio data in terms of Eq. (2), with w=1.8, as means of inferring source geolocation. Note that a simple dipole's endfire null would require w=2.0. This difference between the dipole and the FORTE LPA is due to the LPA's approximate suppression of the "back lobe", that is, of sensitivity to radiation arriving from the anti-nadir direction. This suppression of the backlobe effectively pushes the null angle forward by about 10%.

Figure 7: Measured (vertical axis) versus model (horizontal axis) #1/#2 power ratio based on Eq. (2) with *w*=1.8.
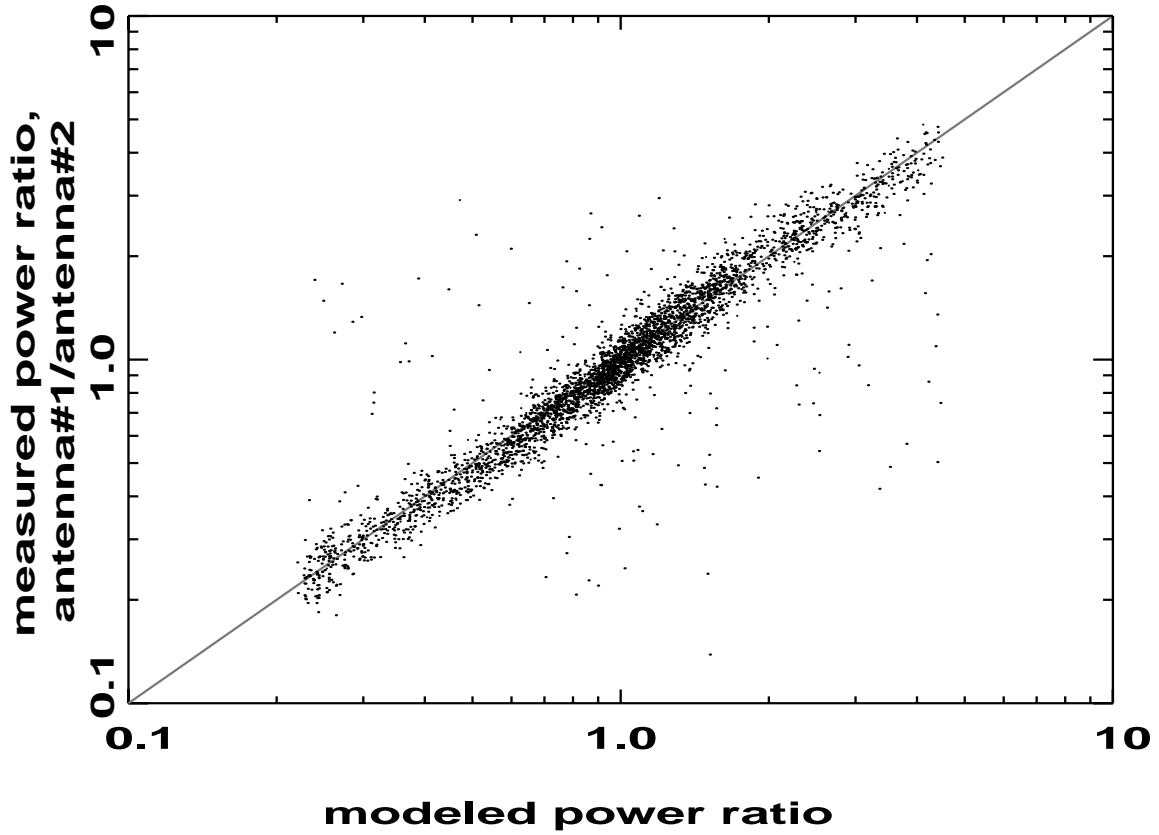

Inferring source geolocations using the empirical power-ratio/principal-angle

relationship

Various treatments of FORTE data have benefited from the use of the total-electron-

content (TEC) signatures to identify clusters of lightning signals probably associated

together in discrete lightning storms [*Jacobson et al.*, 1999; *Jacobson and Shao*, 2001a;

Tierney et al., 2001]. Essentially, the approach is to recognize trends in the TEC as a

function of time. A single storm will have a cluster of events' TEC values arranged along a roughly parabolic TEC-vs-time curve, with the minimum TEC occuring at the satellite's closest approach to the storm. We will now adopt this technique to group events as a cluster from a given storm.

Plate 5 shows the storm-clustering filter, and then geolocation steps, for a marine storm over the Gulf Steam. Plate 5(a) shows the TEC (green and black, for the two antennas) and the inter-antenna power ratio (orange), as a function of time. The vertical axis is logarithmic. The large blue symbols mark TEC points for events that have NLDN coincidence (and hence geolocation.) Plate 5(b) is similar to 5(a) but is selected for a given storm using clustering about a fit based on TEC [*Tierney et al.*, 2001]. The selection based on TEC has eliminated many of the "scattered" points but has retained roughly parabolic clustering (versus time) of either TEC or power ratio.

Plate 5: Illustration of the power-ratio geolocation technique for marine storm off of Nova Scotia. (a) TEC (green and black) and power ratio (orange) on vertical axis, versus time on horizontal axis. Large Blue symbols surround TEC data points having NLDN-furnished geolocation (see text). (b) Same as above, but after selection (see text) for a single storm based on smooth fit to TEC. (c) TEC (green and black) and power ratio (orange) on vertical axis, versus time on horizontal axis, following further selection (see text) to reject power-ratio outliers. The black curve is a fit to the power-ratio data, and the blue triangle is at the minimum of the black curve. The timing and value of that minimum are used to determine the geolocation. (d) Map of the FORTE flight segment (orange diagonal line). The circles are the near-limb (nadir angle =62 deg) limits of satellite visibility at the start (blue), end (green), and storm-closest-approach (orange) points in the flight segment. At storm-closest-approach, there are two points (orange triangles) symettrically separated from the flight segment. The blue squares (completely obscuring the SW orange triangle) are the NLDN geolocations for several of the data points recorded in this flight segment and surviving the selection implemented above.
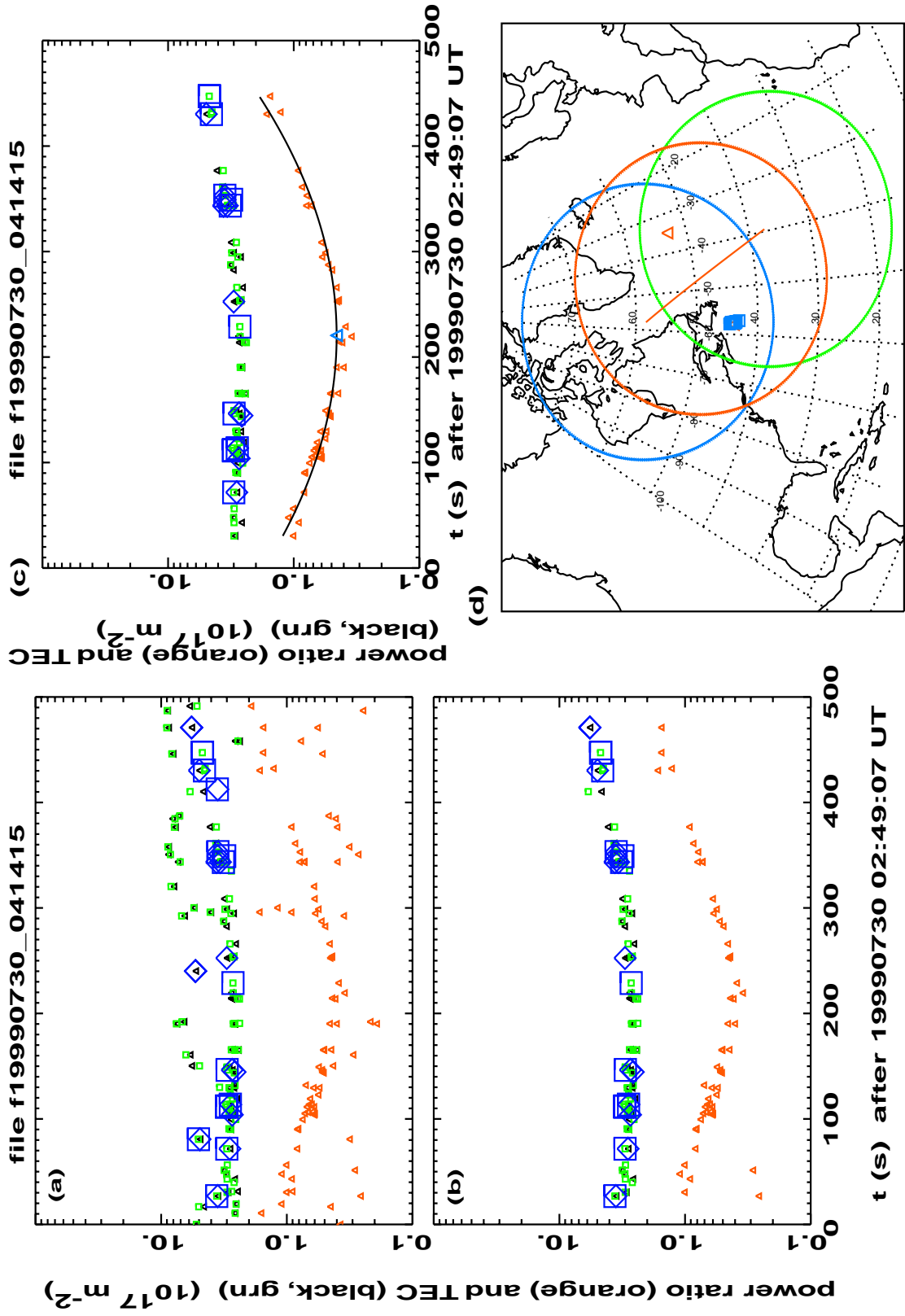
The next step is to fit the power-ratio points to a smooth curve, find the time where that curve minimizes, and find the curve's minimum value. This step is shown in Plate 5(c). All outlier power-ratio points outside a range of 0.1 (in the logarithm base 10) solid-line fit are thrown out; the second iteration of the fit (without outliers) is shown here. The two parameters- time of minimum power ratio, and value of minimum power ratio -together furnish the geolocation. That is shown in Plate 5(d). The orbital pass (diagonal orange line) is a descending one. The upper end and lower end of the orange line in Plate 5(d) correspond to the first and last events, respectively, in the data shown in Plate 5(c). The blue and green circles on the map in Plate 5(d) are the nadir=62 deg loci, for the first and last events, respectively, of Plate 5(c). The orange circle is the circular locus of nadir=62 deg at the time of closest approach to the storm.

In Plate 5(d), the two-fold-ambiguous locations are shown as orange triangles, symmetrically on either side of the satellite track at the time of closest approach. The NLDN geolocations (corresponding to the large blue symbols in Plate 5(c)) are shown as blue squares on the map in Plate 5(d). These geolocations overlay, and mostly obscure, the west geolocation orange triangle from the power-ratio calculation. This both confirms that the power-ratio geolocation agrees with NLDN, and resolves the two-fold ambiguity inherent in the power-ratio data considered alone.

Another example of power-ratio geolocation is shown in Plate 6, which is exactly analogous to Plate 5. One noteworthy difference is that the solution is at the Earth's limb

at earliest and latest times. (The 62-deg circles shown are about 1 deg short of the limb, which is closer to 63 deg.) This means that the series of recorded VHF events spanned the FORTE pass from horizon to horizon, reckoned from the storm location.

Plate 6: Similar to Plate 5, but for a storm off the coast of North Carolina.
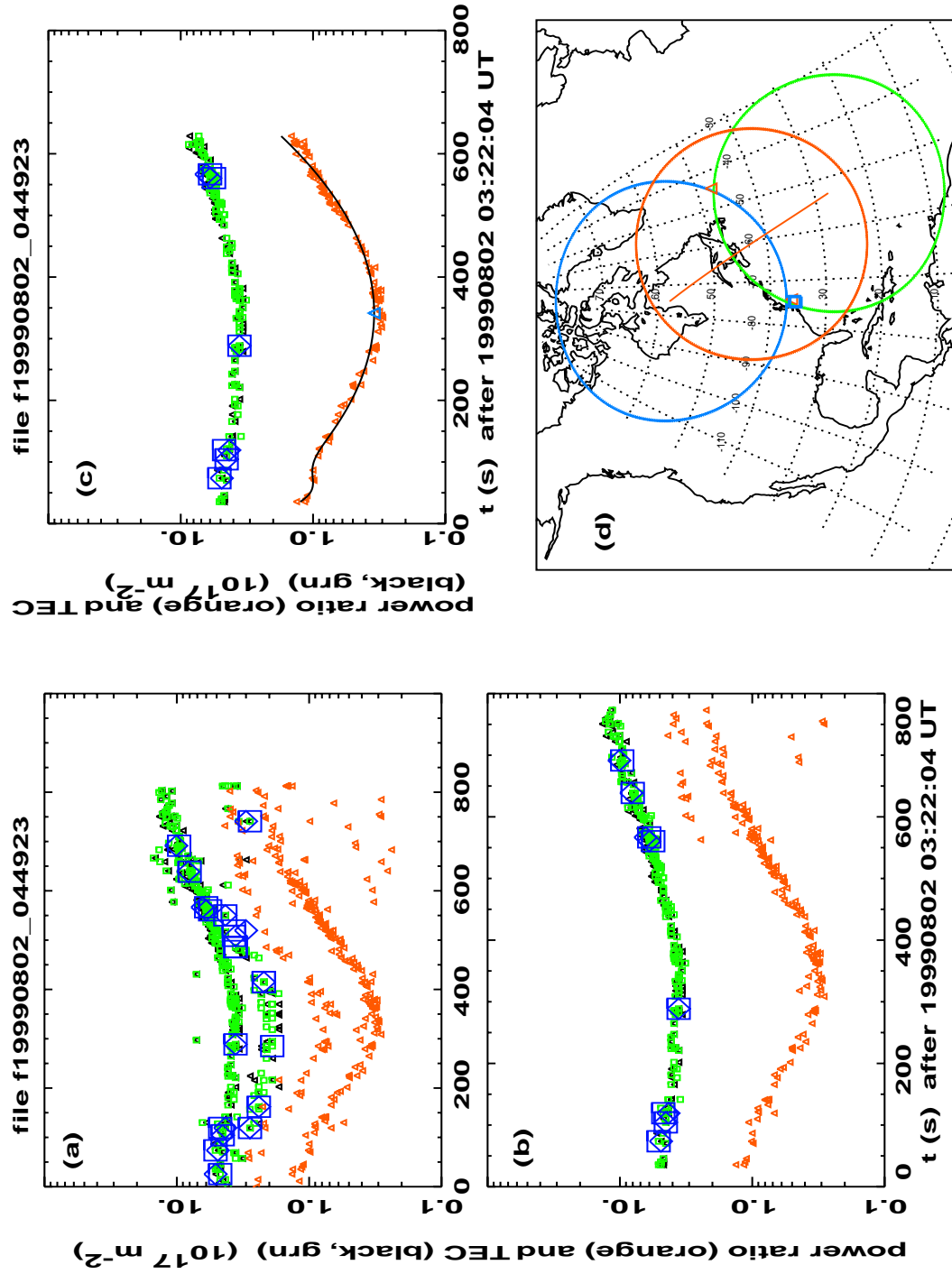
The two examples just treated consist of FORTE VHF data from storms which have *a priori* geolocation already inferred from the VHF events' temporal coincidence [*Jacobson et al.*, 2000] with NLDN. Obviously in such a case the geolocation furnished by the power-ratio method is not only ambiguous, but also, strictly speaking, redundant. However, the purpose for our choosing such examples is to demonstrate that the power-ratio method provides a pair of geolocation points one of which is often in approximate agreement with that inferrred from NLDN.

Accuracy and limitations of the power-ratio geolocation technique

As noted earlier, the power-ratio geolocation technique, without supplementary information, cannot resolve a basic right/left (with respect to the orbit track) positional ambiguity. The two examples shown in Plates 5 and 6 are intended to demonstrate the credible correspondence of one of the right/left symmetric power-ratio geolocations to the NLDN ground-truthing. There are two sources of inaccuracy that tend to complement each other, producing (in the net) a ground-location blur circle on the order of 100-500 km diameter. The first source of inaccuracy is due to the behavior of the function describing the power ratio (see Eq. 2). Its sensitivity to angle *vanishes at nadir* (α_1 and α_2 both 0). On the other hand, the relationship of ground arcdistance (horizonatl distance on the ground) to either of these angles is *most sensitive at nadir*. The second source of inaccuracy is that while, near the Earth's limb (seen from the satellite), the function

(Eq.2) has enhanced sensitivity to nadir angle, i.e. at the limb we are measuring the nadir

angle more sensitively than when α_1 and α_2 are both near 0, nonethless the variation of

ground distance (along the axis leading away from the subsatellite point) is very fast.

This means that a given precision in determining angle gives a worse precision in

determining ground location at the limb than near the subsatellite point. We have

evaluated the joint effect of these two, complementary sources of error in power-ratio

geolocation by looking at >50 cases (of which two were shown in Plates 5 and 6) of

NLDN-groundtruthed geolocations. The empirically determined positional uncertainty is

found in this manner to be on the order of 100-500 km.

In addition to this uncertainty in the geolocation, there are occasional outright mistaken

geolocations, due to mis-identifying as a storm cluster what are really the TEC points

from events deriving from two, widely separated storms. This error propagates into the

power-ratio geolocation and renders it meaningless in those occasional circumstances.

Applications of power-ratio geolocation

Even with the geolocation ambiguity (see Plates 5d and 6d), both the slant distance from

FORTE to the source, and the nadir angle of the source in FORTE coordinates, can be

unambiguously determined for a given storm, as a function of time during the satellite

orbit past the storm. That is, these two parameters do not depend on the right/left

ambiguity of the geolocation. The slant-distance parameter is necessary to convert the
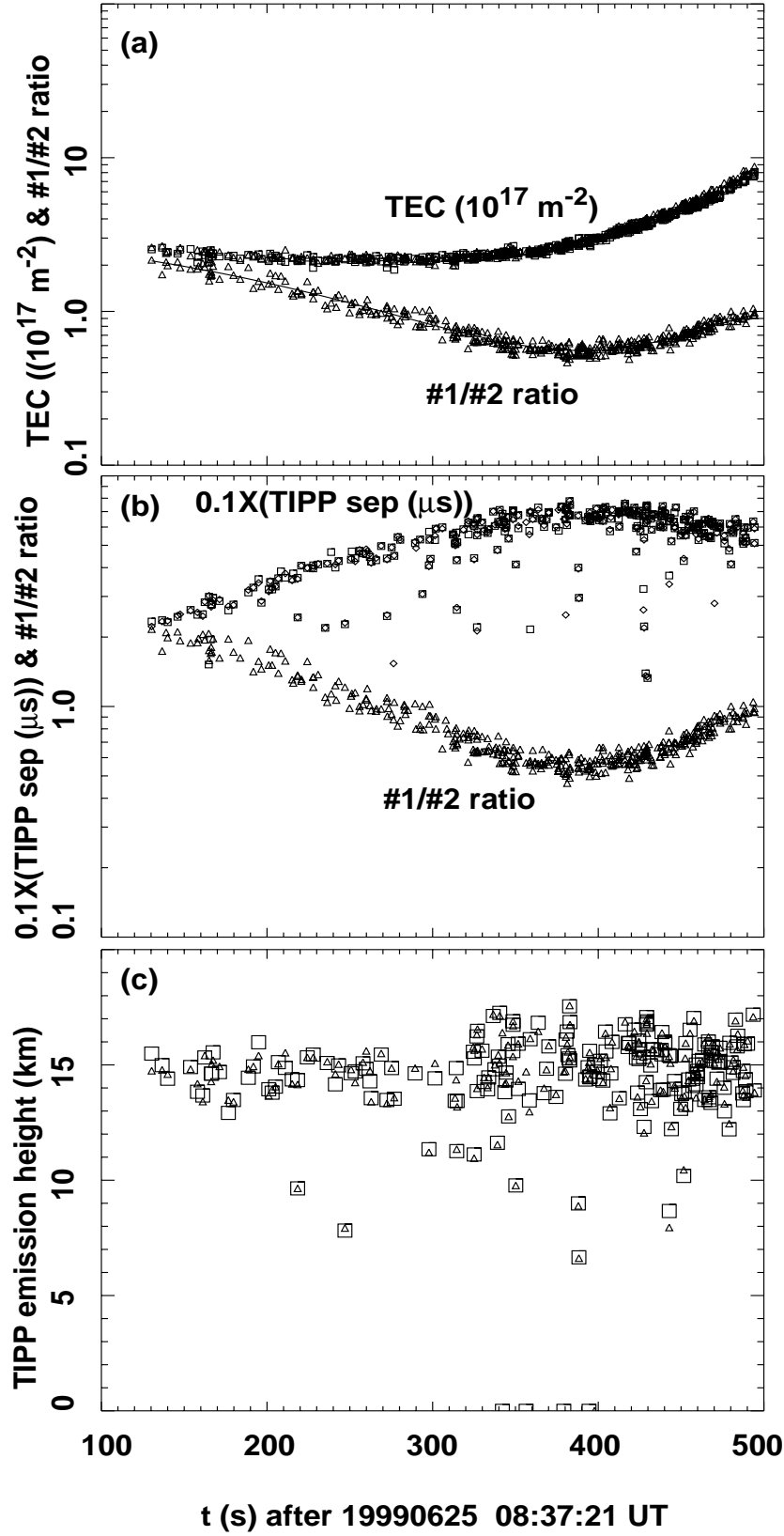
instantaneous received power density into an effective radiated power at the source [*Jacobson et al.*, 2000]. The instantaneous nadir angle is necessary to convert the intra-TIPP separation (in time) to an emission height above the reflective ground [*Jacobson et al.*, 1999]. The emission height in turn allows specification of the portion of a vertically developed convective storm in which the causative electric breakdown is occuring. This may eventually help to identify, via global RF remote-sensing from orbit, those storms that are undergoing deep vertical development.

To illustrate the use of ambiguous geolocation for the analysis of electrical breakdown height above the ground, we will now use a power-ratio geolocation for which there is no corroborating *a priori* (NLDN, optical, etc) geolocation available to resolve the ambiguity. Figure 8 (a) shows the TEC and the #1/#2 power ratio versus time during a FORTE pass over the western Pacific Ocean E/NE of Australia. (Parenthetically, the TEC is a very asymmetric function about the time of closest approach as determined by the power ratio. This is due to strong latitudinal gradients near the ionospheric Appleton anomaly and serves to indicate one of the pitfalls of TEC-based geolocation assuming horizontally-homogenous ionospheric conditions [*Tierney et al.*, 2001].) Figure 8 (b) shows the accompanying TIPP separation (multiplied by 0.1) and, again, the #1/#2 power ratio versus time. The TIPP separation has the characteristic concentration of points near an upper bound, corresponding to the additional delay for RF radiation to reach the satellite via an Earth reflection, as opposed to the direct path to the satellite. The upper bound varies systematically versus time in accord with our expectations based on geometry [*Jacobson et al.*, 1999]. (Basically, the satellite elevation angle maximizes at

the point of closest approach, and goes to zero when the source is at the Earth's limb.)

The TIPP separations are used to retrieve the emission heights (relative to the reflecting

ground) [*Jacobson et al.*, 1999], and these are shown in Figure 8 (c). It is noteworthy that

the heights are clustered around 13-17 km. Is this consistent with other data? The

Tropical Rainfall Measuring Mission (TRMM) satellite's nadir-looking Precipitation

Radar (PR) has shown that tropical/subtropical land- and coastal-storm convective depths

can commonly attain 15 km, in contrast to isolated open-ocean environments where

vertical development is less extreme [*Petersen and Rutledge*, 2001]. Our present example

(Figure 8) of TIPP emission heights is in the coastal regime and consistent with the

TRMM height climatologies.

Figure 8: Analysis of data for blind-geolocation example. (a) TEC and power ratio versus time. (b) 0.1 X (TIPP separation) and power ratio versus time. (c) TIPP-emission height versus time, inferred from the blind geolocation.

(a)

TEC (10^{17} m^{-2})

#1/#2 ratio

(b) 0.1X(TIPP sep (μs))

#1/#2 ratio

(c)

t (s) after 19990625 08:37:21 UT

42

Conclusions and outlook

We have described a novel method for autonomous, single-satellite RF geolocation of electrified convective storms. This method has a positional accuracy of 100-500 km, based on a study set of >50 examples for which we could compare the RF geolocation to external ground-truth location information. Moreover, the method has an intrinsic right-left (with respect to the subsatellite track) location ambiguity.

In the illustrations of the geolocation method, we treated only those satellite flight segments for which the series of power-ratio measurements encompassed the moment of closest approach by the satellite to the storm. We can in principle use Eq. (2) to treat cases in which the satellite's data recording either terminates before closest approach, or alternatively starts after closest approach. In either of these cases, the minimum value of the #1/#2 power ratio cannot be directly measured, but nonetheless the information content of Eq. (2) is such that, when it is fitted to the flight segment's data, we will obtain a geolocation estimate. This estimate will be reliable to the extent that the flight segment is a long one, that is, to the extent that the principal angles α_1 and α_2 are forced to vary widely over the duration of data recording.

A promising use of this technique in future applications will be as an aid in assigning lightning RF-emission sources to meteorological features from other global remote-

sensing products, for example satellite infrared imagery of clouds. In such an application, the imagery will provide clues that resolve the ambiguity. For example, there will in most cases be a feature with cold cloud tops (associated with deep convection and electrification) on only one side, but not the other, of the subsatellite track.

Acknowledgement

References

Boccippio, D.J., K.L. Cummins, H.J. Christian, and S.J. Goodman, Combined satellite- and surface-based estimation of the intracloud-cloud-to-ground lightning ratio over the Continental United States, *Mon. Weath. Rev.*, *129*, 108-122, 2001.

Boccippio, D.J., S.J. Goodman, and S. Heckman, Regional differences in tropical lightning distributions, *J. Appl. Meteor.*, *39*, 2231-2248, 2000.

Boccippio, D.J., W.J. Koshak, H.J. Christian, and S.J. Goodman, Land-ocean differences in LIS and OTD tropical lightning observations, in *11th International Conference on Atmospheric Electricity*, edited by H. Christian, pp. 734-737, National Aeronautics and Space Administration (U. S.), Huntsville, Alabama, 1999.

Born, M., and E. Wolf, *Principles of Optics*, Pergamon Press, Oxford, 1975.

Christian, H.J., R.J. Blakeslee, D.J. Boccippio, W.L. Boeck, D.E. Buechler, K.T. Driscoll, S.J. Goodman, J.M. Hall, W.J. Koshak, D.M. Mach, and M.F. Stewart, Global frequency and distribution of lightning as observed by the Optical Transient Detector (OTD), in *11th International Conference on Atmospheric Electricit*, edited by H. Christian, pp. 726-729, National Aeronautics and Space Administration (U. S.), Huntsville, Alabama, 1999.

Gallimberti, I., The mechanism of the long spark formation, *Journal de Physique*, *40* (7), C7: 193-250, 1979.

Groupe Les Renardieres , Long air gap discharges at Les Renardieres, *Electra*, *35*, 49-156, 1974.

Holden, D.N., C.P. Munson, and J.C. Devenport, Satellite observations of transionospheric pulse pairs, *Geophys. Res. Lett.*, *22* (8), 889-892, 1995.

Jacobson, A.R., K.L. Cummins, M. Carter, P. Klingner, D. Roussel-Dupré, and S.O. Knox, FORTE radio-frequency observations of lightning strokes detected by the National Lightning Detection Network, *J. Geophys. Res.*, *105* (D12), 15,653, 2000.

Jacobson, A.R., S.O. Knox, R. Franz, and D.C. Enemark, FORTE observations of lightning radio-frequency signatures: Capabilities and basic results, *Radio Sci.*, *34* (2), 337-354, 1999.

Jacobson, A.R., and X.-M. Shao, Radiofrequency remote sensing of lightning from space: a study of thunderstorm detectability and lightning discrimination using the FORTE satellite, groundtruthed by NLDN, *J. Geophys. Res.*, *submitted*, 2001a.

Jacobson, A.R., and X.-M. Shao, Using geomagnetic birefringence to locate sources of impulsive, terrestrial VHF signals detected by satellites on orbit, *Radio Science*, *in press*, 2001b.

Light, T.E., D.M. Suszcynsky, and A.R. Jacobson, Coincident Radio Frequency and Optical Emissions from Lightning, Observed with the FORTE Satellite, *J. Geophys. Res.*, *accepted*, 2001.

Massey, R.S., and D.N. Holden, Phenomenology of transionospheric pulse pairs, *Radio Sci.*, *30* (5), 1645-1659, 1995.

Massey, R.S., D.N. Holden, and X.-M. Shao, Phenomenology of trans-ionospheric pulse pairs: Further observations, *Radio Sci*, *33*, 1755-1761, 1998a.

Massey, R.S., S.O. Knox, R.C. Franz, D.N. Holden, and C.T. Rhodes, Measurements of transionospheric radio propagation parameters using the FORTE satellite, *Radio Sci.*, *33* (6), 1739-1753, 1998b.

Petersen, W.A., and S.A. Rutledge, Regional variability in tropical convection: Observations from TRMM, *J. Climate*, *in press*, 2001.

Rhodes, C.T., X.M. Shao, P.R. Krehbiel, R.J. Thomas, and C.O. Hayenga, Observations of lightning phenomena using radio interferometry, *J. Geophys. Res.*, *99*, 13059-13082, 1994.

Shao, X.-M., and A.R. Jacobson, Polarization observations of broadband VHF signals by the FORTE satellite, *Radio Science*, *submitted*, 2001.

Shao, X.M., and P.R. Krehbiel, The spatial and temporal development of intracloud lightning, *J. Geophys. Res.*, *101* (D21), 26,641-26,668, 1996.

Shao, X.M., P.R. Krehbiel, R.J. Thomas, and W. Rison, Radio interferometric observations of cloud-to-ground lightning phenomena in Florida, *J. Geophys. Res.*, *100* (D2), 2,749-2,783, 1995.

Suszcynsky, D.M., M.W. Kirkland, A.R. Jacobson, R.C. Franz, S.O. Knox, J.L.L. Guillen, and J.L. Green, FORTE observations of simultaneous VHF and optical emissions from ligthning: Basic Phenomenology, *J. Geophys. Res.*, *105* (D2), 2191-2201, 2000.

Tierney, H., A.R. Jacobson, W.H. Beasley, and P.E. Argo, Determination of source thunderstorms for VHF emissions observed by the FORTE satellite, *Radio Sci.*, *36* (1), 79, 2001.

Williams, E.R., M.E. Weber, and R.E. Orville, The relationship between lightning type and the convective state of thunderstorms, *J. Geophys. Res.*, *94*, 13213-13220, 1989.